IOP Publishing Journal of Physics: Condensed Matter
J. Phys.: Condens. Matter **32** (2020) 145901 (8pp) https://doi.org/10.1088/1361-648X/ab61cb

Kinetic Monte Carlo simulations of the dynamics of a coupled system of free and localized carriers in AlGaN

O Kravcov, J Mickevičius and G Tamulaitis

Institute of Photonics and Nanotechnology, Vilnius University, Saulėtekio al. 3, LT-10257, Vilnius, Lithuania

E-mail: kravcovas@gmail.com and juras.mickevicius@ff.vu.lt

Received 20 September 2019, revised 29 November 2019
Accepted for publication 12 December 2019
Published 8 January 2020

Abstract

A model for the dynamics of a coupled system of free and localized carriers in semiconductors with strong carrier localization is suggested. Kinetic Monte Carlo technique is exploited for simulations. The model is verified by fitting the simulated and experimental temperature dependences of photoluminescence (PL) band intensity, peak position, and band width, and the carrier density dependence of PL efficiency in AlGaN quantum wells. The influence of carrier localization conditions on the dominating carrier migration and recombination processes is revealed. The efficiency droop effect is shown to be caused by peculiarities of carrier localization without significant influence of Auger recombination.

Keywords: AlGaN, carrier localization, Monte Carlo simulations, efficiency droop

(Some figures may appear in colour only in the online journal)

1. Introduction

Spatial band gap variations due to inhomogeneities in composition, quantum well (QW) thickness, and strain strongly affect the performance of photonic devices based on ternary and quaternary III-nitride alloys. Localization of the nonequilibrium carriers at the minima of the potential fluctuations can be beneficial for the light emission efficiency: localized carriers are isolated from nonradiative recombination centers (NRCs) [1, 2], and high internal quantum efficiency (IQE) can be achieved despite the large dislocation densities [3, 4]. On the other hand, the carrier localization influences the carrier dynamics even at high densities of nonequilibrium carriers [5–15]. The localization affects the radiative and Auger recombination rates [5, 6]. Delocalization-activated nonradiative recombination and incomplete carrier localization have been suggested as the efficiency droop mechanisms [7–11]. The band potential fluctuation profile has been shown to influence the stimulated emission threshold [12–14]. The carrier localization might also induce current crowding and premature device degradation [15].

Experimentally, the potential fluctuations are evident by a strong inhomogeneous broadening of the photoluminescence (PL) spectra [16]. Additionally, the carrier localization induces unusual temperature dependences of the PL band peak position and width: S-shaped and W-shaped dependences, respectively, have been observed for InGaN [6, 17–19] and AlGaN [7, 12, 14, 16, 20, 21] alloys. The spatial variations of emission intensities and/or peak positions have been studied directly by confocal microscopy [2, 11, 22], scanning near-field optical microscopy (SNOM) [1, 15, 23, 24], and cathodoluminescence (CL) [9, 25]. The potential fluctuations on several spatial scales were revealed with the largest domains of a micron size and the smallest on the scale of a few nm [25–27].

The dynamics of nonequilibrium carriers in the localizing potential is that of the coupled system of the localized and free carriers. However, due to the random nature of the band potential fluctuations, modeling of the carrier dynamics within the localizing potential is a formidable task. Usually, it requires solving the Schrödinger equation for electrons and holes in random localizing potential and determining the energies and

the spatial structure of the localized quantum states. Recently, a method based on localization landscape theory has been proposed, which somewhat reduces the complexity by replacing the Schrödinger equation with a simpler one [28–30].

Simplified approaches to modeling the system consisting of free and localized carriers are typically based on reducing the system to a single dominant constituent of either free or localized carriers at certain conditions. The former are analyzed using the standard ABC model [31–34] with modified recombination rates to allow for the localized carrier migration and recombination [9–11] and/or excitonic recombination [35, 36]. This model relies on the statistical averages describing the thermalized distributions of carriers. Alternatively, for the case of dominant population of localized carriers, Monte Carlo simulations of exciton hopping through a random localizing potential are used [18, 19, 21, 37]. This approach fails at high carrier densities when the contribution of free carriers becomes significant as well as at high temperatures when carriers easily delocalize.

The current study is aimed at developing a method combining both approaches, which is capable of modeling the free and localized carriers simultaneously. Exploiting the kinetic Monte Carlo simulation technique, we were able to describe the temperature- and excitation-dependent behavior of PL band in wide-band-gap AlGaN QWs structure with strong carrier localization. The simultaneous fit of these dependences has been used as a figure of merit for validation of the model and the parameters used in the model. The simulations enabled us to reveal the importance of certain carrier migration and recombination mechanisms for the dynamics of the coupled system of free and localized carriers in a wide temperature range. In particular, it is shown that the efficiency droop at elevated excitations in AlGaN QWs used for fitting in this study can be caused by peculiarities of carrier localization without a significant contribution of the Auger processes.

2. Kinetic Monte Carlo simulations

In our model, we consider the following carrier subsystems: free electrons and holes, and exciton-like localized electron–hole pairs. The free carriers can move independently, whereas, the excitons are supposed to behave like single particles that can be trapped by localizing potential [18, 37].

The localized carriers (excitons) can recombine radiatively, hop to another localized state or to the mobility edge (and become delocalized), or tunnel to NRC. The rate of the radiative recombination is calculated as an inverse of the exciton radiative lifetime:

$$\nu_{\mathrm{rad}} = \frac{1}{\tau_{\mathrm{rad}}}. \tag{1}$$

The hopping rate from site i to site j is calculated according to the well-known Miller-Abrahams formula:

$$\nu_{i\to j} = \nu_0 \exp\left(-\frac{2R_{ij}}{\alpha}\right) \exp\left(-\frac{(E_j - E_i) + |E_j - E_i|}{2k_{\mathrm{B}}T}\right), \tag{2}$$

where E_i and E_j are the energies of the initial and final states, respectively, R_{ij} is the distance between the states in space, α is the decay length of exciton wavefunction, ν_0 is the attempt-to-escape frequency, k_{B} is the Boltzmann constant, and T is the temperature. The exciton hopping takes place only to an unoccupied localized state.

Carrier delocalization occurs as a transition to mobility edge at the rate:

$$\nu_{\mathrm{deloc}} = \nu_{\mathrm{d}} \exp\left(-\frac{\Delta E}{k_{\mathrm{B}}T}\right). \tag{3}$$

Here, $\Delta E = E_{\mathrm{me}} - E_i$ is the energy difference between mobility edge E_{me} and localized state E_i, and ν_{d} is the attempt-to-delocalize frequency, which is similar to ν_0, but includes also the rate of exciton dissociation as well as reflects the probabilities to hop above the mobility edge and relax to it.

The rate of exciton tunneling to NRCs depends on the spatial distribution of both localized states and NRCs, and can be calculated using equation (2) under assumption that the energies of all NRCs serving as the final state E_j are equal. The contribution of all NRCs have to be included:

$$\nu_{\mathrm{nonrad}} = \sum_{\mathrm{NRCs}} \nu_{i\to\mathrm{NRC}}. \tag{4}$$

The total decay rate of an exciton at a given localized state is calculated as:

$$\nu_i = \nu_{\mathrm{rad}} + \sum_{j\neq i} \nu_{i\to j} + \nu_{\mathrm{deloc}} + \nu_{\mathrm{nonrad}}. \tag{5}$$

The free carriers are also handled as single particles, but within a large ensemble. Since the carrier thermalization is assumed to be much faster than the recombination and localization processes, the carrier–carrier and carrier–phonon interactions are neglected. The energy distribution of the thermalized ensemble is described by the Fermi–Dirac distribution function $f(E; E_{\mathrm{F}})$, where E_{F} is the quasi-Fermi level energy.

The free carriers can move in space, recombine radiatively or nonradiatively, or become localized. Since the spatial distribution of carriers is random, the diffusion processes can be neglected, and the random motion of carriers is simulated as the movement of independent Brownian particles with thermal velocity v_{th}. As the processes of recombination and localized exciton formation require the participation of both electron and hole, we calculate the transition rates for electrons and assume that the required hole emulates the same behavior.

The bimolecular radiative recombination rate for a single electron is calculated as:

$$\nu_{\mathrm{bimol}} = Bp, \tag{6}$$

where p is the free hole concentration, and B is the bimolecular recombination coefficient. The nonradiative recombination rate is expressed using Shockley–Read–Hall model as:

$$\nu_{\mathrm{SRH}} = v_{\mathrm{th}} N_{\mathrm{t}} \sigma_{\mathrm{t}}, \tag{7}$$

where N_{t} and σ_{t} are the density and cross-section of NRCs, respectively. The capture of free carriers to the localized state is similar to exciton hopping down to lower energy state, except that only the unoccupied localized states within the

Table 1. Dynamic processes included in the calculations of event rate. The numbers in parentheses indicate the equations used to calculate the corresponding rate.

Localized carriers (excitons)			Free carriers		
Radiative linear recombination	ν_{rad}	(1)	Radiative bimolecular recombination	ν_{bimol}	(6)
Nonradiative recombination	ν_{nonrad}	(4)	Nonradiative recombination	ν_{SRH}	(7)
Delocalization	ν_{deloc}	(3)	Capture to a localized state	ν_{cap}	(8)
Hopping	$\nu_{i\to j}$	(2)			

radius R_{loc} are considered and both electrons and holes must be present nearby. The capture rate in this case can be calculated as:

$$\nu_{\text{cap}} = \nu_{\text{cap0}} \sum_{j,R_j<R_{\text{loc}}} \exp\left(-\frac{R_j}{R_{\text{loc}}}\right), \tag{8}$$

where ν_{cap0} is the capture rate in the limit of carriers being at the same place as the localized state. The total decay rate of a free electron is calculated as:

$$\nu_{\text{free}} = \nu_{\text{bimol}} + \nu_{\text{SRH}} + \nu_{\text{cap}}. \tag{9}$$

The summary of the dynamic processes included in the calculations of carrier decay rates is provided in table 1.

The simulations of carrier dynamics were performed using kinetic Monte Carlo algorithm and following the flow chart shown in figure 1. The detailed simulation procedure is as follows.

(i) 4D space-energy grid with three spatial dimensions and one energy dimension is created. The grid size is $128 \times 128 \times 5 \times 1000\,\text{nm}^3$ meV. The localized states with density N_{loc} and nonradiative recombination centers with density N_{t} are generated randomly within the grid. The energies of the localized states are chosen in such a way that a Gaussian density of localized states is obtained. No correlation between the energies of the localized states and their spatial positions is allowed.

(ii) Free carriers are generated randomly within the grid. To make the simulations closer to steady-state conditions, the carrier generation is uniformly distributed in time, instead of generating all free carriers at time $t = 0$. For the instantaneous free carrier concentration n_{free}, the quasi-Fermi level E_{F} is calculated using the equation:

$$n_{\text{free}} = \int_0^\infty g(E)\, f(E; E_{\text{F}})\, \text{d}E, \tag{10}$$

where $g(E)$ is the density of states for the free carriers. Random energy values are assigned to the free carriers according to the Fermi–Dirac distribution $f(E; E_{\text{F}})$.

(iii) A particle is randomly selected. The rates of all possible transition are calculated, as described above. The probability of any event happening is calculated using the expression:

$$W = 1 - \exp(-\nu \Delta t), \tag{11}$$

where ν is the total decay rate ν_{free} or ν_i for a free carrier or a localized exciton, respectively, and Δt is the time step. A random number taken from a uniform distribution between 0 and 1 determines the event occurrence. If no event occurs, the free carrier moves randomly in space, and the next particle is picked. Otherwise, the type of the process is determined using another random number and the decay rates described by equations (5) and (9) for excitons and free carriers, respectively. After the particle state update, the procedure is repeated to check for the second successive event during the same time step. To reduce the probability of such events, the time step is chosen small enough. If the process of radiative recombination takes place, the spatial coordinates, time moment, and energy of the emitted photon are all recorded.

(iv) Step (iii) is repeated for all the particles. Afterwards, a new time step begins: a new portion of free carriers is generated, and the procedure is repeated from step (ii), until the final time step value is reached.

(v) For a new simulation cycle, a new grid with a different random distribution of localized states is generated by starting the procedure from step (i).

The PL spectrum is accumulated by summing the contribution of each radiative recombination event. To obtain each PL spectrum, the simulations were repeated with 10 000 different grids. The time step of 1 ps was selected, since it acceptably reduces the probability of a second successive event for a particle during a single time step. The evolution of the system was simulated for 5000 time steps (or 5 ns), which is sufficient to achieve an equilibrium state in a quasi-steady-state excitation regime.

To fit the experimental dependences with the simulation results, the excitation power densities are converted to the carrier generation rates. The fitting range covers 5 orders of magnitude from 1.2×10^{25} to 3.9×10^{30} $\text{cm}^{-3}\ \text{s}^{-1}$ in generation rate, corresponding to the calculated carrier density between 2×10^{15} and 2.4×10^{20} cm^{-3}. The essential parameters used in our simulations are $\nu_0\tau_{\text{rad}}$, $\nu_{\text{d}}\tau_{\text{rad}}$, $\nu_{\text{cap0}}\tau_{\text{rad}}$, $N_{\text{loc}}\alpha^3$, and $N_{\text{t}}\sigma_{\text{t}}$. To estimate the value of $\nu_0\tau_{\text{rad}}$, we assumed that ν_0 is of the order of $10^{12}\ \text{s}^{-1}$ [38]. According to the typical experimental results, the exciton lifetime in AlGaN MQWs was taken to be 200 ps [39], which gives $\nu_0\tau_{\text{rad}} = 200$. The other parameters were obtained by fitting multiple experimental dependences simultaneously, as described below. The low-temperature bimolecular recombination coefficient B was equal to 4×10^{-10} $\text{cm}^3\ \text{s}^{-1}$ [40], and its dependence on

carrier density due to degeneracy was taken into account as $B = B_0/(1 + n/n^*)$ [31]. Here, B_0 is the low-density coefficient, and n^* is the carrier density at saturation threshold equal to 3×10^{19} cm^{-3}. The values of all the parameters are listed in table 2.

3. Experimental details

To study the dense carrier system containing significant fractions of both localized and free carriers, PL measurements have been carried out on AlGaN/AlGaN multiple quantum wells (MQWs) structure exhibiting strong carrier localization. The AlGaN/AlGaN MQWs were grown by migration-enhanced metalorganic chemical vapor deposition (MEMOCVD®) technique on a *c*-plane sapphire substrate. Ten pairs of 5.0 nm thick $Al_{0.35}Ga_{0.65}N$ quantum wells separated by 11.5 nm thick $Al_{0.49}Ga_{0.51}N$ barriers were grown on a 1.2 μm thick *n*-$Al_{0.55}Ga_{0.45}N$ buffer layer.

The PL spectra were measured under excitation power density varied from 0.4 kW cm^{-2} to 14 MW cm^{-2} at different temperatures from 8 K to 300 K. The 4th harmonic (266 nm) of the Q-switched YAG:Nd laser radiation (pulse duration 4 ns) was used for excitation under quasi-steady-state conditions. A closed-cycle helium cryostat ensured the variation and stabilization of temperature. The PL signal was analyzed by a double monochromator (Jobin Yvon HRD-1) and detected by a UV-enhanced photomultiplier.

4. Results and discussion

The simulations of carrier dynamics using the model we developed in this work require many material parameters and several assumptions on the processes of importance. To make the fitting of experimental and simulated results more reliable, we simultaneously fitted two groups of experimentally obtained dependences: (i) temperature dependences of PL efficiency, PL band peak position, and PL band width measured at fixed (low) excitation power density; and (ii) PL efficiency dependences on excitation power density measured at different temperatures. These dependences are commonly used to evaluate various material parameters. The PL efficiency dependence on temperature is usually exploited for the estimation of the IQE under assumption that the efficiency is 100% at low temperatures, even though this assumption is not always true [41]. The S-shaped PL band peak position and W-shaped PL band width dependences indicate carrier localization, and are typically used to quantify the band potential fluctuation profile [6, 7, 12, 14, 16–21]. The PL efficiency dependences on excitation power density generally exhibit efficiency droop, and are used to evaluate the contribution of Auger recombination [31, 33], which is commonly accepted as the main origin of the efficiency droop in InGaN materials [42, 43], and has been suggested to be important also in AlGaN [33]. Nevertheless, the Auger processes have also been shown to be affected by carrier localization [5, 6, 34], while recently, the importance of carrier localization to efficiency droop has reemerged [30, 44, 45]. This situation motivated us for an attempt to simulate

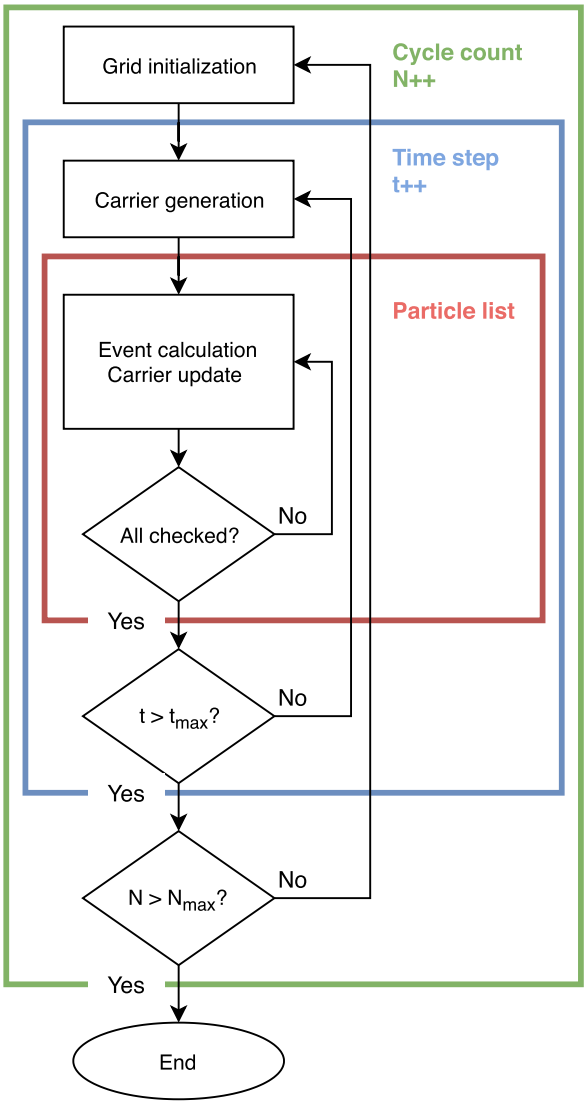

Figure 1. The flow chart of simulation algorithm.

the carrier dynamics in AlGaN by properly describing the influence of carrier localization and without the involvement of the Auger processes.

The starting point in the simulations of PL properties is reproducing the PL spectrum at the conditions corresponding to those in experiment. The PL spectra measured at low temperatures have a Gaussian-like band with strongly expressed LO phonon replicas, as shown in figure 2(a). At elevated temperatures, the phonon replicas become less distinct due to homogeneous thermal broadening (see figure 2(b)). At low excitations, the high-energy slope of the PL band is governed only by the distribution of localized states and exhibits no change with increasing excitation, whereas at high carrier densities, the slope is also affected by the free carrier distribution. Moreover, the increasing excitation results in free carrier heating, which also changes the high-energy slope of the PL band. The typical experimental and simulated PL spectra are illustrated in figure 2 for the temperatures of 8 K and 300 K.

The next step is modeling the temperature dependences of the PL band properties. The experimentally obtained temperature dependence of the spectrally-integrated PL intensity is

Table 2. Values of parameters used in simulations.

Parameter	Value	Parameter	Value	Parameter	Value
τ_{rad}	200 ps	N_{loc}	10^{19} cm^{-3}	σ	30 meV
$\nu_0\tau_{rad}$	200	N_t	3×10^{16} cm^{-3}	Γ	26 meV
$\nu_d\tau_{rad}$	2000	$N_t\sigma_t$	300 cm^{-1}	$\hbar\omega_{LO}$	98 meV
$\nu_{cap0}\tau_{rad}$	6	B_0	4×10^{-10} cm^3 s^{-1}	β	0.04 meV K^{-1}
$N_{loc}\alpha^3$	10	n^*	3×10^{19} cm^{-3}	γ	0.75 eV

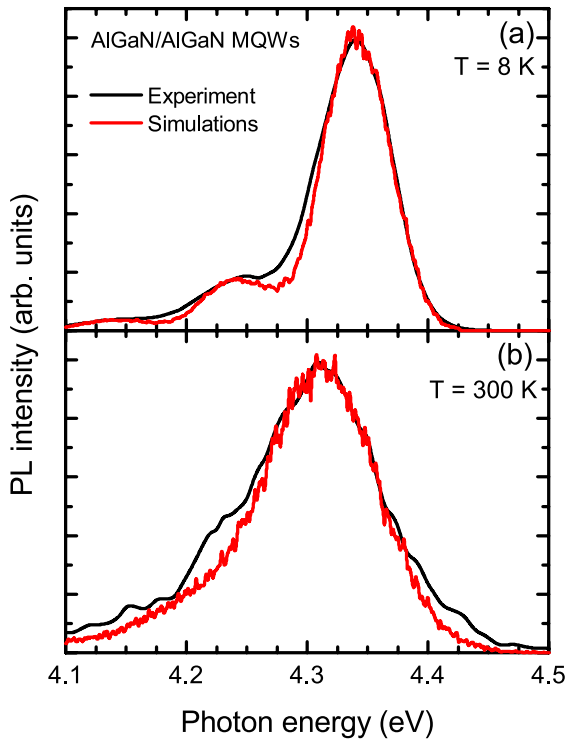

Figure 2. Experimental (black) and simulated (red) PL spectra of AlGaN MQWs at 8 K (a) and 300 K (b) temperatures.

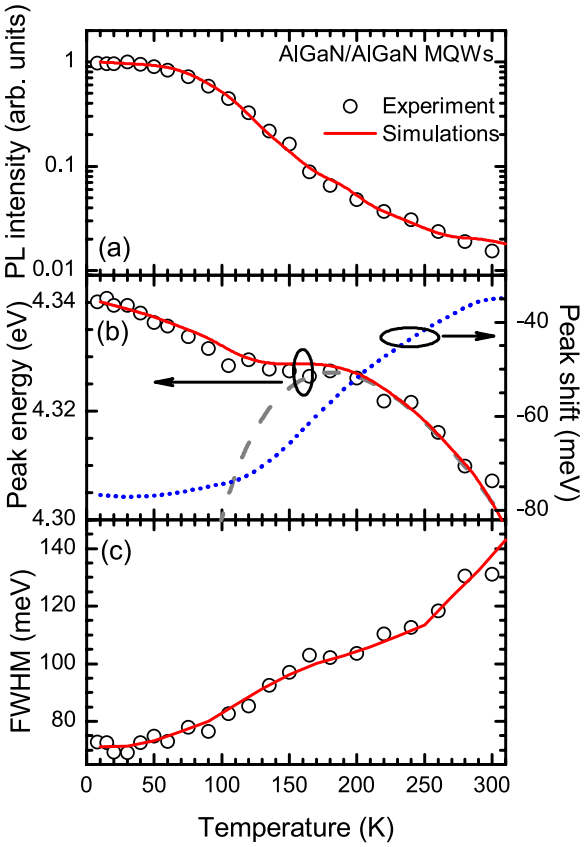

Figure 3. Experimental (points) and simulated (line) PL efficiency (a), band peak position (b), and band width (c) dependences on temperature in AlGaN MQWs under study. The gray dashed line and the blue dotted line in (b) illustrate, respectively, the peak position calculated using Eliseev formula [17] and the peak position shift with respect to that at 0 K after subtracting the band gap shrinkage (see details in text).

presented by points in figure 3(a). The PL intensity is almost constant at temperatures below ~40 K and decreases by two orders of magnitude as the temperature is increased up to room temperature. The solid line in figure 3(a) represents the simulated dependence, which fits fairly well. The modeling revealed that the IQE equals ~90% at low temperature and decreases down to less than 1% at room temperature. The PL efficiency decrease with temperature is caused by the increasing fraction of free carriers as well as by an increasing rate of nonradiative recombination.

The temperature dependence of the PL band peak position, shown by filled points in figure 3(b), exhibits nonmonotonous S-shape behavior with three shift regions: initial red shift up to 100 K, followed by a flat region in the range between 100 K and 180 K, and a red shift again at elevated temperatures. Such behavior is typical for ternary III-nitrides and indicates carrier (exciton) redistribution through the localized states [7, 14, 16–21]. At the lowest temperatures, the carriers are frozen at the localized states they occupy after relaxation from excited states, since the thermally-activated redistribution has low probability. Nevertheless, they are still able to hop to adjacent lower-energy states by tunneling. The initial increase in temperature facilitates the carrier redistribution to the lowest available states. The further temperature increase leads to thermalization of the carriers and a blue shift of the band, which results in a more or less pronounced dip in the S-shaped dependence. The PL band red shift at elevated temperatures is caused by the band gap shrinkage.

The high-temperature region of the peak position dependence can be adequately described by the Eliseev formula [17], as shown by the dashed line in figure 3(b), which provides the localization parameter $\sigma = 30$ meV reflecting the energy dispersion of localized states. Meanwhile, subtracting the band gap shrinkage calculated by the Varshni formula [46] with parameters $\alpha = 1.04$ meV K^{-1} and $\beta = 888$ K [47] and plotting the peak position shift with respect to the band gap energy

at 0 K (4.417 eV) reveals that the difference between the PL band and the band gap is constant up to ~100 K temperature. This behavior, shown by open triangles in figure 3(b), indicates that most carriers (excitons) occupy the lowest energy states even at the temperatures as low as 8 K. Moreover, the initial difference of 77 meV is substantially larger than the energy dispersion of localized states (30 meV). Thus, the carriers at low temperatures occupy localized states deep on the tail of the Gaussian distribution. The simulated dependences using these insights and the localization parameter $\sigma = 30$ meV are shown by solid lines in figure 3(b). The fit of simulated results with the experimental data is fairly good in the entire temperature range.

The measured temperature dependence of the PL band width is shown by points in figure 3(c). It exhibits a W-shaped behavior, as is usual for the strong influence of carrier localization [18, 19, 21]. The PL band width varies little below 60 K, increases with temperature until ~160 K, remains constant until ~200 K, and increases again at higher temperatures. The first major increase in PL band width is caused by increasing ability of localized carriers (excitons) to occupy higher energy states. The kink at ~160 K represents a crossover from a non-thermalized to a thermalized energy distribution of the excitons, while the constant band width above the crossover is an indication that a thermalized exciton energy distribution is established. Finally, the second increase in PL band width at elevated temperatures is due to strengthening carrier-phonon interaction [19].

The simulations of PL band width dependence on temperature revealed that the simple localization model, described by a single parameter σ, is insufficient, thus, a more sophisticated double-scaled potential profile model was used. According to this model [18, 19, 21–24], localized carriers (excitons) experience potential fluctuations with the dispersion parameter σ within a certain macroscopically large-scale spatial region. The average exciton energy of such regions fluctuates on another energy scale with dispersion parameter Γ. Under the assumption that the carrier redistribution between the separate large-scale regions is negligible, the dynamics of the PL band peak position is governed mostly by the small-scale potential fluctuations, whereas, the PL band width is a result of the convolution of the distributions reflecting fluctuations on both scales. As shown by the solid line in figure 3(c), the best fit was achieved using the parameters $\sigma = 30$ meV and $\Gamma = 26$ meV. The phonon-assisted band broadening $\Delta\Phi$ has been taken into account as follows [48, 49]:

$$\Delta\Phi(T) = \beta T + \frac{\gamma}{\exp\left(\frac{\hbar\omega_{LO}}{k_B T}\right) - 1}. \qquad (12)$$

Here β and γ represent the coupling strength of carriers (excitons) with acoustic and LO phonons, respectively. We use $\hbar\omega_{LO} = 98$ meV, $\beta = 0.04$ meV K^{-1} and $\gamma = 0.75$ eV obtained from the linear interpolation between the values for GaN and AlN [49].

Finally, the excitation power density dependences of PL efficiency at different temperatures were simulated by taking into account the localizing potential landscape. The PL efficiency was calculated as the ratio of spectrally-integrated PL intensity and excitation power density. As illustrated by points in figure 4, the experimental dependences have two regions: a small initial increase, and the droop at elevated excitations. The droop onset shifts to lower excitations as the temperature is decreased. The solid lines in figure 4 represent the simulated dependences, which quite adequately follow the experimentally observed behavior for the selected value of localized state density $N_{loc} = 10^{19}$ cm^{-3}.

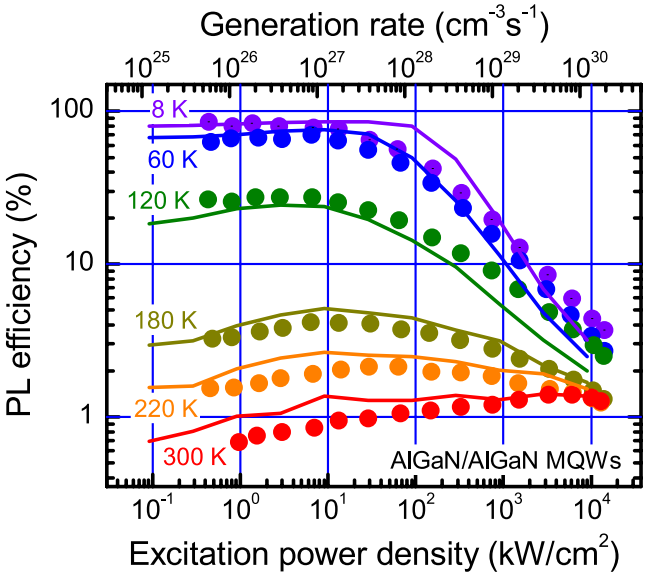

Figure 4. The measured and simulated PL efficiency dependences on excitation power density (points) and carrier generation rate (lines), respectively, at different temperatures (indicated).

The initial increase of PL efficiency is typically attributed to several effects: the saturation of NRCs, the increasing role of bimolecular radiative recombination due to filling of localized states, and the screening of built-in electric field in QWs [11, 41, 45]. Likewise, the efficiency droop is also assigned to several competing mechanisms with Auger recombination and carrier delocalization being the most important [4, 7–11, 14, 31, 33, 41, 42, 44]. Both for efficiency increase and decrease, the main factor governing the PL efficiency is the ratio between the densities of localized and free carriers: the free carriers recombine radiatively via the more effective bimolecular-type transitions, however, are vulnerable to nonradiative recombination, conversely, the localized carriers are less susceptible to nonradiative recombination, but their radiative recombination is linear. This ratio depends on the localizing potential landscape, and recently, we have proposed a parameter $k_B T/\sigma$, which reflects the ability of localized carriers to delocalize and migrate, and determines the droop mechanism [14, 44]. However, this parameter does not provide details on the contributions of different mechanisms. The simulated excitation and temperature dependences of the ratio between localized and free carrier densities are presented in figure 5. As can be observed, the carriers are mostly localized at temperatures below 100 K, and only at elevated excitations,

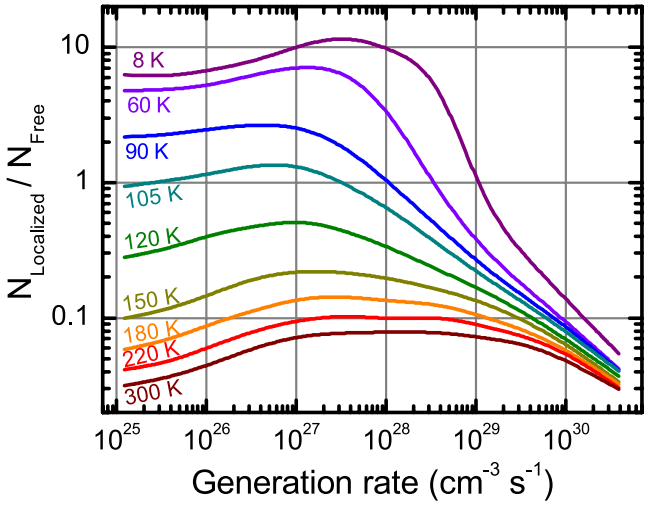

Figure 5. Simulated dependences of the ratio between localized and free carrier densities on generation rate at different temperatures.

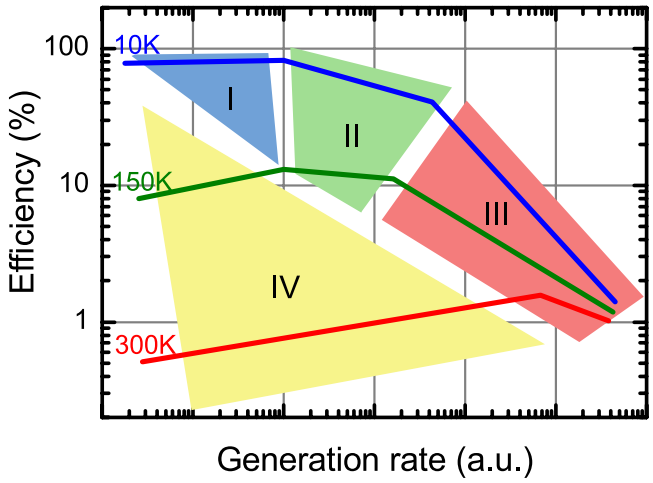

Figure 6. Main regions of the PL efficiency dependences reflecting specific dynamics of nonequilibrium carriers.

once the localized states start saturating, the free carriers become a dominant fraction. Furthermore, at low excitations, the fraction of localized carriers increases with excitation even at temperatures as high as 300 K.

The results of our simulations allowed us to divide the generation rate dependences of the PL efficiency at different temperatures into four areas reflecting the dominance of certain processes in the dynamics of nonequilibrium carriers. Figure 6 presents the division schematically.

In area I, most of the carriers are deeply localized and, as a result, are well isolated from NRCs. The radiative recombination of localized carriers (excitons) controls the PL spectrum and intensity. IQE is high, weakly depends on temperature, and is limited by the ratio between the rates of carrier capture to the localized states and to the NRCs. The density of localized states and radiative lifetime of localized carriers (excitons) determine the range of this area at fixed temperature.

In area II, the efficiency droop emerges due to the nonradiative recombination of localized carriers deteriorating the efficiency. Besides, the fraction of free carriers starts increasing, even though still remaining minor. The onset of area II indicates the ability of excitons to reach NRCs, whereas the slope depends on the NRC density. Nevertheless, the slope remains smaller than that in the area III.

Area III corresponds to the efficiency droop. At elevated excitations, the localized states start saturating, thus, the fraction of free carriers rapidly increases and becomes dominant. However, the free carrier nonradiative recombination dominates over bimolecular recombination, which is still lower than the radiative recombination from localized carriers (excitons).

Area IV is the area exhibiting an increase in efficiency at increasing excitation. Since carrier capture occurs only to those localized states, which have both electron and hole nearby, the increasing carrier density results in the higher probability of carrier localization. As the delocalization rate at fixed temperature is almost constant, it ensues the rising fraction of localized carriers even at 300 K temperature, and causes the efficiency increase.

All the data discussed above imply that the major contribution to photon generation is from localized carriers (excitons) even at room temperature and high generation rate. Despite the considerable increase in free carrier density at elevated excitations, the dominant nonradiative recombination ensures that the role of bimolecular recombination remains smaller than that of the radiative recombination of localized carriers. The PL efficiency dynamics reflects the changes in the relative rates of recombination due to these mechanisms.

5. Conclusions

Kinetic Monte Carlo simulations applied for the system consisting of localized and free carriers enables evaluating the contributions and rates of the main processes determining the efficiency droop, temperature dependence of luminescence efficiency, and the shape of temperature dependences of luminescence band parameters. It has been shown that the efficiency droop in such a system can be interpreted without significant influence of Auger recombination and is mainly determined by peculiarities of carrier localization. The droop effect is attributed to the transition of the system of nonequilibrium carriers from the state with the dominant light emission from strongly localized states with weak nonradiative recombination to the state of predominantly free carriers with a high rate of nonradiative recombination and still a low rate of radiative bimolecular recombination. Excellent agreement between theoretical simulations and experimental data was obtained by employing the developed model for AlGaN QWs with high density of localized states. The model and simulation procedures are applicable for analysis of carrier dynamics in any materials, where localized and free carriers coexist.

Acknowledgments

The research was funded by European Social Fund (Project No. LMT-K-712-01-0076) under grant agreement with the Research Council of Lithuania (LMTLT).

ORCID iDs

O Kravcov https://orcid.org/0000-0001-7148-3335
J Mickevičius https://orcid.org/0000-0003-1623-4138

References

[1] Hitzel F, Klewer G, Lahmann S, Rossow U and Hangleiter A 2005 *Phys. Rev.* B **72** 081309
[2] Kaneta A, Funato M and Kawakami Y 2008 *Phys. Rev.* B **78** 125317
[3] Chichibu S, Azuhata T, Sota T and Nakamura S 1996 *Appl. Phys. Lett.* **69** 4188
[4] Shatalov M, Yang J, Sun W, Kennedy R, Gaska R, Liu K, Shur M and Tamulaitis G 2009 *J. Appl. Phys.* **105** 073103
[5] Jones C M, Teng C-H, Yan Q, Ku P-C and Kioupakis E 2017 *Appl. Phys. Lett.* **111** 113501
[6] Shahmohammadi M, Liu W, Rossbach G, Lahourcade L, Dussaigne A, Bougerol C, Butte R, Grandjean N, Deveaud B and Jacopin G 2017 *Phys. Rev.* B **95** 125314
[7] Mickevičius J, Tamulaitis G, Shur M, Shatalov M, Yang J and Gaska R 2013 *Appl. Phys. Lett.* **103** 011906
[8] Bochkareva N, Rebane Y T and Shreter Y G 2013 *Appl. Phys. Lett.* **103** 191101
[9] Wang J, Wang L, Wang L, Hao Z, Luo Y, Dempewolf A, Muller M, Bertram F and Christen J 2012 *J. Appl. Phys.* **112** 023107
[10] Hader J, Moloney J V and Koch S W 2010 *Appl. Phys. Lett.* **96** 221106
[11] Lin Y, Zhang Y, Liu Z, Su L, Zhang J, Wei T and Chen Z 2014 *J. Appl. Phys.* **115** 023103
[12] Mickevičius J, Jurkevičius J, Kazlauskas K, Žukauskas A, Tamulaitis G, Shur M S, Shatalov M, Yang J and Gaska R 2012 *Appl. Phys. Lett.* **101** 041912
[13] Pecora E F, Zhang W, Nikiforov A Yu, Zhou L, Smith D J, Yin J, Paiella R, Dal Negro L and Moustakas T D 2012 *Appl. Phys. Lett.* **100** 061111
[14] Mickevičius J, Jurkevičius J, Tamulaitis G, Shur M S, Shatalov M, Yang J and Gaska R 2014 *Opt. Express* **22** A491
[15] Pinos A, Marcinkevičius S, Yang J, Bilenko Y, Shatalov M, Gaska R and Shur M S 2009 *Appl. Phys. Lett.* **95** 181914
[16] Kuokstis E, Sun W H, Shatalov M, Yang J W and Asif Khan M 2006 *Appl. Phys. Lett.* **88** 261905
[17] Eliseev P G, Perlin P, Lee J and Osinski M 1997 *Appl. Phys. Lett.* **71** 569
[18] Kazlauskas K, Tamulaitis G, Pobedinskas P, Žukauskas A, Springis M, Huang C-F, Cheng Y-C and Yang C C 2005 *Phys. Rev.* B **71** 085306
[19] Ozaki T, Funato M and Kawakami Y 2017 *Phys. Rev.* B **96** 125305
[20] Bell A, Srinivasan S, Plumlee C, Omiya H, Ponce F A, Christen J, Tanaka S, Fujioka A and Nakagawa Y 2004 *J. Appl. Phys.* **95** 4670
[21] Kazlauskas K, Žukauskas A, Tamulaitis G, Mickevičius J, Shur M S, Fareed R S Q, Zhang J P and Gaska R 2005 *Appl. Phys. Lett.* **87** 172102
[22] Mickevičius J, Dobrovolskas D, Aleknavičius J, Grinys T, Kadys A and Tamulaitis G 2018 *J. Lumin.* **199** 379
[23] Pinos A, Liuolia V, Marcinkevičius S, Yang J, Gaska R and Shur M S 2011 *J. Appl. Phys.* **109** 113516
[24] Marcinkevičius S, Jain R, Shatalov M, Yang J, Shur M and Gaska R 2014 *Appl. Phys. Lett.* **105** 241108
[25] Iwata Y, Oto T, Gachet D, Banal R G, Funato M and Kawakami Y 2015 *J. Appl. Phys.* **117** 115702
[26] Hahn W *et al* 2018 *Phys. Rev.* B **98** 045305
[27] Oliver R A, Bennett S E, Zhu T, Beesley D J, Kappers M J, Saxey D W, Cerezo A and Humphreys C J 2010 *J. Phys. D: Appl. Phys.* **43** 354003
[28] Filoche M, Piccardo M, Wu Y-R, Li C-K, Weisbuch C and Mayboroda S 2017 *Phys. Rev.* B **95** 144204
[29] Piccardo M, Li C-K, Wu Y-R, Speck J S, Bonef B, Farrell R M, Filoche M, Martinelli L, Peretti J and Weisbuch C 2017 *Phys. Rev.* B **95** 144205
[30] Li C-K, Piccardo M, Lu L-S, Mayboroda S, Martinelli L, Peretti J, Speck J S, Weisbuch C, Filoche M and Wu Y-R 2017 *Phys. Rev.* B **95** 144206
[31] Piprek J 2010 *Phys. Status Solidi* a **207** 2217
[32] Hopkins M A, Allsopp D W E, Kappers M J, Oliver R A and Humphreys C J 2017 *J. Appl. Phys.* **122** 234505
[33] Nippert F, Mazraehno M T, Davies M J, Hoffmann M P, Lugauer H-J, Kure T, Kneissl M, Hoffmann A and Wagner M R 2018 *Appl. Phys. Lett.* **113** 071107
[34] Nippert F, Karpov S Yu, Callsen G, Galler B, Kure T, Nenstiel C, Wagner M R, Strassburg M, Lugauer H-J and Hoffmann A 2016 *Appl. Phys. Lett.* **109** 161103
[35] Haughn C R, Rupper G, Wunderer T, Yang Z, Johnson N M, Wraback M and Garrett G A 2019 *Appl. Phys. Lett.* **114** 102101
[36] Langer T, Chernikov A, Kalincev D, Gerhard M, Bremers H, Rossow U, Koch M and Hangleiter A 2013 *Appl. Phys. Lett.* **103** 202106
[37] Baranovskii S D, Eichmann R and Thomas P 1998 *Phys. Rev.* B **58** 13081
[38] Baranowski M, Kudriawiec R, Luce A V, Latkowska M, Yu K M, Kuang Y J, Misiewicz J, Tu C W and Walukiewicz W 2015 *J. Appl. Phys.* **117** 175702
[39] Mickevičius J, Tamulaitis G, Kuokštis E, Liu K, Shur M S, Zhang J P and Gaska R 2007 *Appl. Phys. Lett.* **90** 131907
[40] Podlipskas Ž, Aleksiejūnas R, Kadys A, Mickevičius J, Jurkevičius J, Tamulaitis G, Shur M, Shatalov M, Yang J and Gaska R 2016 *J. Phys. D: Appl. Phys.* **49** 145110
[41] Mickevičius J, Tamulaitis G, Shur M, Shatalov M, Yang J and Gaska R 2012 *Appl. Phys. Lett.* **101** 211902
[42] Iveland J, Martinelli L, Peretti J, Speck J S and Weisbuch C 2013 *Phys. Rev. Lett.* **110** 177406
[43] Delaney K T, Rinke P and Van de Walle C G 2009 *Appl. Phys. Lett.* **94** 191109
[44] Mickevičius J, Jurkevičius J, Kadys A, Tamulaitis G, Shur M, Shatalov M, Yang J and Gaska R 2016 *AIP Adv.* **6** 045212
[45] Gfroerer T H, Chen R, Watt G, Liu Z and Zhang Y 2019 *J. Appl. Phys.* **125** 204502
[46] Varshni Y P 1967 *Phys. Status Solidi* **19** 459
[47] Nepal N, Li J, Nakarmi M L, Lin J Y and Jiang H X 2005 *Appl. Phys. Lett.* **87** 242104
[48] Rudin S, Reinecke T L and Segall B 1990 *Phys. Rev.* B **42** 11218
[49] Nam K B, Li J, Lin J Y and Jiang H X 2004 *Appl. Phys. Lett.* **85** 3489